Journal of Nondestructive Evaluation (2026) 45:44
https://doi.org/10.1007/s10921-026-01341-x

Sizing Wedge Delaminations Using Lock-in Thermography

José C. Ciria-Cosculluela[1] · Jon Pérez-Arbulu[2] · Agustín Salazar[3] · Ricardo Celorrio[4] · Arantza Mendioroz[3]

Received: 24 November 2025 / Accepted: 15 February 2026

Abstract
Sizing hidden defects is a major challenge in many industries. In the last years we have successfully used optically excited lock-in infrared thermography to size the geometrical parameters of both infinite and semi-infinite uniform delaminations. In this work, we study more realistic flaws, by dealing with wedge delaminations of continuously varying width, depth, thickness and combination of two of them. As these parameters vary slowly, the previously developed analytical model for semi-infinite delamination remains valid. We present experimental data taken by applying lock-in infrared thermography on stainless steel samples containing calibrated wedge delaminations. The resulting amplitude and phase thermograms are fitted to the analytical model to obtain the parameters describing the geometry of the delaminations. The agreement found between the retrieved geometry and the true varying parameters strengthens lock-in infrared thermography as a powerful tool to size hidden defects.

Keywords Lock-in infrared thermography · Delaminations · Thermal resistance · Defect detection · Quantitative thermography · Nondestructive testing

1 Introduction

Delaminations refer to flat subsurface flaws oriented parallel to the sample surface. They are recurrent defects in layered metals and composites, reducing the material stiffness and the structures' reliability [1, 2]. Optically excited infrared thermography (IRT) is a very powerful technique for detection and characterization of hidden defects [3–5]. In this technique, a light beam illuminates the sample surface while an IR video camera records the evolution of the surface temperature. Roughly speaking, abnormal features in the surface temperature reveal the presence of subsurface defects. The main advantages of IRT are its non-contact (both excitation and detection) and non-destructive nature. Moreover, no sample preparation is needed. Sometimes, just reversible black painting of the surface to enhance light absorption and IR emission is used. Accordingly, IRT is specially well adapted to deal with real parts in industrial environments. In fact, for decades, optically excited IRT has been extensively applied to detect delaminations; see Ref. [6] and the references therein for a recent review on this subject and Ref. [7] for latest experimental approaches.

Lock-in IRT, which uses an intensity modulated light beam, is the ideal illumination scheme for scouting the sizing limits (deepest, thinnest and/or narrowest delamination), because it provides low noise thermograms. The lock-in analysis of the IR film recorded for several illumination periods delivers amplitude and phase thermograms with reduced statistical noise [8].

In the last years, in our laboratory we have used optically excited lock-in IRT to size the morphological parameters of delaminations with increasing geometrical complexity. As a first step, we studied infinite and homogeneous delaminations, i.e. delaminations of very large area featuring uniform thickness [9]. Using the analytical expression of the surface temperature we obtained successfully the depth and thickness of calibrated

✉ Arantza Mendioroz
arantza.mendioroz@ehu.eus

[1] Departamento de Informática e Ingeniería de Sistemas, Universidad de Zaragoza, Facultad de Ciencias, C/Pedro Cerbuna 12, 50009 Zaragoza, Spain

[2] Departamento de Matemática Aplicada, Escuela de Ingeniería de Gipuzkoa-Eibar, Universidad del País Vasco UPV/EHU, Av. Otaola 29, 20600 Eibar, Spain

[3] Departamento de Física Aplicada, Escuela de Ingeniería de Bilbao, Universidad del País Vasco UPV/EHU, Plaza Ingeniero Torres Quevedo 1, 48013 Bilbao, Spain

[4] Departamento de Matemática Aplicada, EINA/IUMA, Universidad de Zaragoza, Campus Río Ebro, Edificio Torres Quevedo, 50018 Zaragoza, Spain

Published online: 06 March 2026

delamination. In a second step, we studied semi-infinite delaminations, i.e. rectangular delaminations of infinite length and finite width [10, 11], still featuring uniform thickness. In this 2D problem, the surface temperature was calculated analytically using the thermal quadrupoles formalism [12–15]. Then, as an extension of the previous work on 2D delaminations, we studied semi-infinite delaminations with non-uniform transverse thickness, i.e. thickness variation along the delamination width [16]. In all cases, the method was assessed on metallic samples with calibrated delaminations.

In this work, we take a step forward to approach realistic delaminations but keeping both simple geometries and analytical solutions of the surface temperature, we study semi-infinite wedge delaminations. This means that the rectangular delamination has infinite length and continuously varying width, depth or thickness. Moreover, we also include combined variations of depth and thickness. This configuration has two advantages. On the one hand, as these parameters vary slowly, the previously developed analytical model for semi-infinite delaminations [10] remains valid. On the other hand, it is possible to manufacture metallic samples with calibrated wedge delaminations.

We perform optically excited lock-in IRT experiments on a set of calibrated wedge delaminations, i.e. we control at micrometric level the dimensions of the three geometrical parameters: width, depth and thickness. Then, by fitting the analytical expression of the surface temperature to the experimental data to obtain the three unknown geometrical parameters. We verify that they agree very well with the nominal parameters, confirming optically excited IRT as an invaluable tool for NDT testing of subsurface delaminations.

2 Theory

Figure 1a shows the cross-section of an opaque sample of thermal diffusivity D, with a buried delamination. The sample is infinitely long in the y and z directions whereas in x direction its size is L. The 2D delamination is very long in the y direction and is defined by the following geometrical parameters: width w, thickness t and depth d beneath the surface. We consider that a CW uniform laser beam of intensity I_0, modulated at frequency $f(\omega = 2\pi f)$, illuminates the sample. Heat losses from all sample surfaces are neglected.

The oscillating component of the temperature, $\tau(x, z)$, resulting from the modulated excitation of the flawed specimen can be obtained by solving the following partial derivative differential equation:

$$\frac{\partial^2 \tau_i}{\partial x^2} + \frac{\partial^2 \tau_i}{\partial z^2} - \frac{j\omega}{D}\tau_i = 0, i = 1,2 \tag{1}$$

with sample boundary conditions corresponding to the incident flux, $I_o/2$ at the illuminated surface ($z=0$), and adiabatic boundary conditions at the rest of the sample surfaces.

The geometry for modelling the problem is sketched in Fig. 1b. The delamination is modelled as a bounded thermal contact resistance $R(x)$ that keeps flux continuity. For modelling purposes, the sample is divided into two layers: layer 1 above the horizontal through the delamination and layer two below the delamination. The thermal contact resistance results in a temperature discontinuity boundary condition at the delamination:

$$\tau_1(z = d) - \tau_2(z = d) = R(x)\varphi_z(x, d) \tag{2}$$

where φ_z is the heat flux perpendicular to the interface.

The distribution of thermal resistance values in the x direction, $R(x)$, representing a delamination of uniform thickness

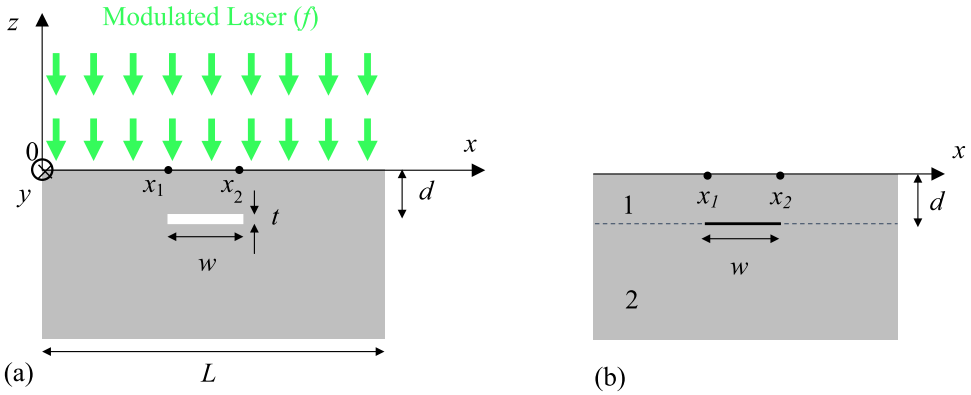

Fig. 1 (**a**) Diagram of the cross-section of a 2*D* delamination of width w, thickness t and depth d, and infinite length (y direction) located inside an opaque sample. The sample is very long in the y and z directions and has a size L in the x direction. (**b**) Sketch of the geometry for modelling: the sample is divided into two layers of the same material, 1 above- and 2 below the horizontal through the delamination. The delamination is modelled as an interface with a given thermal resistance R

bounded between x_1 and x_2, such as the one depicted in Fig. 1a, can be written as

$$R(x) = R\,for\,x_1 < x < x_2 \tag{3a}$$

$$R(x) = 0\,for\,x < x_1\,and\,x > x_1 \tag{3b}$$

Assuming the delamination is filled with air, the contact resistance R is related to the delamination thickness by: $R = t/K_{air}$, where K_{air} is the thermal conductivity of the air [17].

The solution to this problem was obtained analytically in Ref. [10], by means of the thermal quadrupoles method [12] and the cosine Fourier transform of the x-coordinate [18]. In the following, we summarize the main steps of the calculation. First, an x-coordinate cosine Fourier transform is applied on the temperature $\tau(x,z)$,

$$\theta(\alpha_n, z) = \int_0^L \tau(x,z)cos(\alpha_n x)dx,\ with\,\alpha_n = \frac{n\pi}{L}\ and\ n \in N \tag{4}$$

which transforms Eq. (1) into an ordinary differential equation on the transformed temperature:

$$\frac{d^2\theta_i}{dz^2} - \gamma_n^2\theta_i = 0 \tag{5}$$

where $\gamma_n^2 = \alpha_n^2 + j\omega/D$

The boundary conditions also need to be transformed. In particular, the transformation of the temperature discontinuity (Eq. (2)) writes:

$$\Delta\theta_{Rn} = \theta_1(\alpha_n, d) - \theta_2(\alpha_n, d) = \int_0^L R(x)\varphi_z(x,d)cos(\alpha_n x)dx \tag{6}$$

Equation 6 represents the transform of the product $R(x)\varphi_z(x,y)$. The transforms of these individual functions can be expressed as:

$$\rho(\alpha_n) = \rho_n = \int_0^L R(x)cos(\alpha_n x)dx \tag{7a}$$

$$\Phi_R(\alpha_n) = \Phi_{Rn} = \int_0^L \varphi_z(x,d)cos(\alpha_n x)dx \tag{7b}$$

In turn, the inverse of the transformed resistance distribution writes:

$$R(x) = \sum_{k=0}^{\infty} g_k(x)\rho(\alpha_k),\ with \qquad g_k(x) = \begin{matrix} \frac{1}{L} & \text{for } k = 0 \\ \frac{2}{L}cos(\alpha_k x) & \text{for } k \neq 0 \end{matrix} \tag{8}$$

and the inverse of the transformed heat flux perpendicular to the interface as

$$\varphi_z(x,d) = \sum_{m=0}^{\infty} g_m(x)\Phi_R(\alpha_m),\ with \qquad g_m(x) = \begin{matrix} \frac{1}{L} & \text{for } m = 0 \\ \frac{2}{L}cos(\alpha_m x) & \text{for } m \neq 0 \end{matrix} \tag{9}$$

According to these expressions, Eq. (6) results in:

$$\Delta\theta_{Rn} = \sum_{m=0}^{\infty}\Phi_{Rm}\sum_{k=0}^{\infty}\int_0^L \rho(\alpha_k)g_k(x)g_m(x)cos(\alpha_n x)dx = \sum_{m=0}^{\infty}\Phi_{Rm}N_{\rho m} \tag{10}$$

Then, application of the images method enables relating the temperature and heat flux at the front and rear surfaces of the sample in a matrix form, and simplifies the analytical expression of the transformed surface temperature $\theta_1(0)$:

$$\theta_1(0) = \left[A_1A_2 + B_1C_2 + A_1N_\rho C_2\right]\left[C_1A_2 + A_1C_2 + C_1N_\rho C_2\right]^{-1}\Phi_1(0) \tag{11}$$

Here, $\Phi_1(0)$ is $I_oL/2$, and A_i, B_i and C_i are diagonal square matrices of size $N+1$ whose coefficients are $\cosh(\gamma_n d_i)$, $\sinh(\gamma_n d_i)/(K\gamma_n)$ and $K\gamma_n\sinh(\gamma_n d_i)$, respectively, N being large enough for the thermal resistance distribution expressed in Eq. (8) to converge to the true distribution with $2N+1$ harmonics.

Finally, N_ρ is an $N \times N$ matrix whose coefficients are obtained from Eq. (10)

$$N_\rho = \frac{1}{L}\begin{pmatrix} \rho_o & 2\rho_1 & 2\rho_2 & .... & 2\rho_N \\ \rho_1 & \rho_o + \rho_2 & \rho_1 + \rho_3 & .... & \rho_{N-1} + \rho_{N+1} \\ \rho_2 & \rho_1 + \rho_3 & \rho_0 + \rho_4 & .... & \rho_{N-2} + \rho_{N+2} \\ .... & .... & .... & .... & .... \\ \rho_N & \rho_{N-1} + \rho_{N+1} & \rho_{N-2} + \rho_{N+2} & .... & \rho_o + \rho_{2N} \end{pmatrix} \tag{12}$$

From Eqs. (3) the elements forming matrix N_ρ take the form,

$$\rho_o = R(x_2 - x_1) \tag{13a}$$

$$\rho_n = \frac{R}{\alpha_n}\left[sin(\alpha_n x_2) - sin(\alpha_n x_1)\right] \text{for } n \neq 0 \tag{13b}$$

Finally, the inverse cosine Fourier transform of the surface temperature $\theta_1(0)$ is calculated to obtain the surface temperature $\tau_1(x,0)$.

$$\tau_1(x,0) = \frac{1}{L}\theta_1(\alpha_o, 0) + \frac{2}{L}\sum_{n=1}^{\infty}\theta_1(\alpha_n, 0)cos(\alpha_n) \tag{14}$$

As in this work we are studying wedge delaminations, featuring slightly and continuously varying geometrical properties (w,d,t), the 2D model remains valid. Although we cannot quantify the slope of these "slightly varying" geometrical properties, since it would require calculations using a 3D model, we estimate that they are valid provided the slope is smaller than ten degrees.

Finally, we will work with the normalized surface temperature, $\tau_n(x)$, obtained as the ratio of $\tau(x)$ and the surface temperature at any sound location (see Eq. 2.22 in Ref. [19])

$$\tau_\infty = \frac{I_o}{2\varepsilon\sqrt{\omega}} e^{-i\frac{\pi}{4}} \tag{15}$$

where ε is the thermal effusivity of the sample [20, 21]. Equation (15) shows the well-known −45° phase delay between the excitation and the surface temperature. We will obtain the geometrical parameters describing the delamination as a function of the y axis by fitting surface temperature x profiles measured at different locations along the y axis.

3 Experimental Results

3.1 Experimental Setup and Calibrated Samples

The experimental lock-in infrared thermography setup used in this work is depicted in Fig. 2. The surface of the sample is illuminated by a CW diode laser beam ($\lambda = 808$ nm, up to 50 W), fiber coupled, with nominal "top hat" profile. The defocused beam intensity actually decreases from center to border. To overcome this issue, we placed a beam homogenizer at the end of the fiber head. By modulating the electric current that feeds the laser driver we modulate the laser output.

The radiation coming from the sample surface is collected and recorded by an infrared video camera (X6800 from FLIR, NEDT 20 mK, detector 640 × 512 px). The camera is equipped with a 50 mm focal length lens and a 2 cm long extension ring providing a spatial resolution of 89 µm per pixel. A dedicated software performs a lock-in analysis of the IR images delivering the amplitude and phase distribution of the surface temperature oscillations.

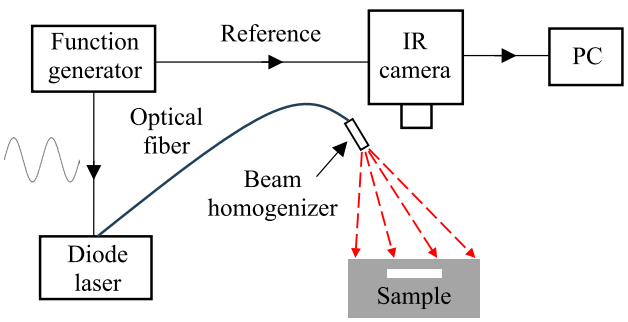

Fig. 2 Diagram of the experimental lock-in infrared thermography setup

The camera records images for 60 s at a frame rate of 50 images/s, i.e., 3000 images at each frequency. As the noise level is inversely proportional to the square root of the total number of images [7] the average noise in temperature is below 1 mK. Finally, we normalize the data by dividing the amplitude and subtracting the phase by the corresponding values at locations distant from the delamination.

We manufactured samples containing calibrated delaminations by eroding U-shaped through-thickness notches in parallelepiped blocks made of AISI-304 stainless steel. The delaminations were simulated by manufacturing an independent insert of the same material tightly adapted to the notch. By using metallic films between U-shaped block and insert we control the delamination thickness (the thickness of the embedded air layer). In fact, we measure the width, the depth and the thickness of the delamination using different callipers, with a precision of 0.1 mm, 0.01 mm and 1 µm, respectively. In all cases we focus on thin delaminations ($t < 100$ µm) to assess lock-in IRT for early detection of inner defects. The sample was covered by a thin layer of graphite aimed at enhancing absorption of the laser radiation and IR emission. This layer can be easily removed by applying a safe solvent such as isopropyl alcohol. In the case of porous samples, a thin black tape (e.g. 5 µm thick) can be pasted on the sample surface which can be easily removed after the experiments. In the following subsections we will describe separately the geometry of each of the wedge delaminations we worked with, together with the thermographic measurements performed on them.

Although most delaminations appear in composite materials, we perform our experiments in stainless steel since it is easier to manufacture calibrated features in this material with micrometric precision. Anyway, the results can be extrapolated to composites just considering their lower thermal diffusivity.

For all samples studied in this work, we took data at several frequencies verifying that the thermal diffusion length $\left(\mu = \sqrt{D/(\pi f)}\right)$ for AISI-304 stainless-steel was long enough for the thermal waves to reach the delamination.

3.2 Delamination with Wedge Width

The geometry of this delamination is shown in Fig. 3. The insert is tightly introduced in the notch of U-shaped cross-section, whose width varies monotonically. In this way, we obtain a calibrated delamination with fixed depth ($d = 1$ mm) and continuously varying width (from $w = 10$ mm to 2 mm). To control the uniform thickness of the delamination, i.e. the thickness of the air layer between the notch and the insert, we put two metallic films of known thickness ($t = 20$ µm) at both ends of the U-shaped wedge hole.

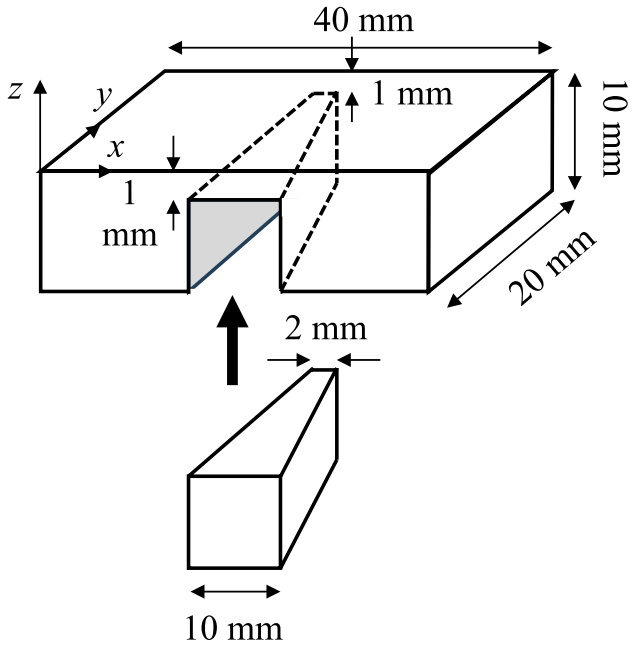

Fig. 3 Scheme of the AISI-304 stainless-steel U-shaped piece together with the tightly inserted part to obtain a calibrated delamination with wedge width from 10 to 2 mm

As an example, we show in Fig. 4 the amplitude and phase thermograms obtained at $f = 0.3$ Hz. Note that the wedge width of the delamination is clearly detected. Then, in order to size the three geometrical parameters defining the delamination we select several temperature profiles along the x direction through different y coordinates. Finally, we fit each x-profile to the analytical model (see Eq. (16) in Ref. 10) to obtain simultaneously w, d and t. We average the results obtained at four frequencies (0.3, 0.4, 0.55 and 0.7 Hz) to obtain the mean value and the standard deviation. In Fig. 5a we show in dots five experimental temperature x-profiles at different y positions for $f = 0.4$ Hz together with the fits to the model (continuous lines). Figure 5b shows by dots the retrieved values of the three parameters of the delamination and by continuous straight lines the nominal values. Note the overall good agreement between nominal and measured values. Regarding the width, it follows the lineal trend except for narrow delaminations, where the effect of the thermal resistance due to the lateral walls of the artificial delamination cannot be neglected. On the other hand, the depth is slightly overestimated and the thickness slightly underestimated. Anyway, it is quite impressive how the delamination thickness, which is the most hidden parameter and therefore the less sensitive quantity [22], is quite well estimated.

For the sake of consistency, we have followed the same protocol for the same sample with $t = 50$ μm. We have found very similar results, which are not shown here so as not to lengthen the manuscript unnecessarily.

3.3 Delamination with Wedge Thickness

Now we consider a U-shaped notch of constant width ($w = 10.0$ mm) and depth ($d = 1.02$ mm) but monotonously varying the thickness of the air layer from 0 to 25 μm, as shown in Fig. 6. To achieve this configuration, we insert a parallelepiped block, which is kept in direct contact with the notch at one end, but separated by 25 μm at the other end by means of a metallic film of such thickness.

Following the same steps as in the previous subsection, we show in Fig. 7 amplitude and phase thermograms recorded at $f = 0.3$ Hz. Note that a variation of the contrast in both thermograms along the y-direction is visually distinguished, but it is not possible to ascribe it to t or d wedges.

Following the same procedure as in subSect. 3.2, we characterize the three geometrical parameters of the delamination by selecting several temperature profiles across the delamination, which are fitted to the analytical model to obtain w, d and t, simultaneously. We average the results obtained at the four frequencies (0.3, 0.4, 0.55 and 0.7 Hz) from which we calculate the mean value and the standard deviation. In Fig. 8a we show five temperature profiles across the delamination at different y positions at $f = 0.4$ Hz. Dots are the data and the continuous lines are the fit to the model. Figure 8b shows by dots the retrieved values of the three parameters of the delamination and by continuous straight lines the nominal values.

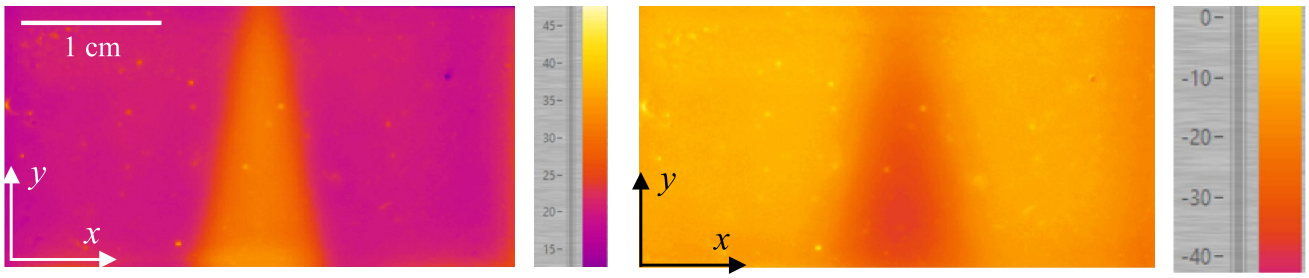

Fig. 4 Amplitude (left) and phase (right) thermograms at $f = 0.3$ Hz for the sample outlined in Fig. 3

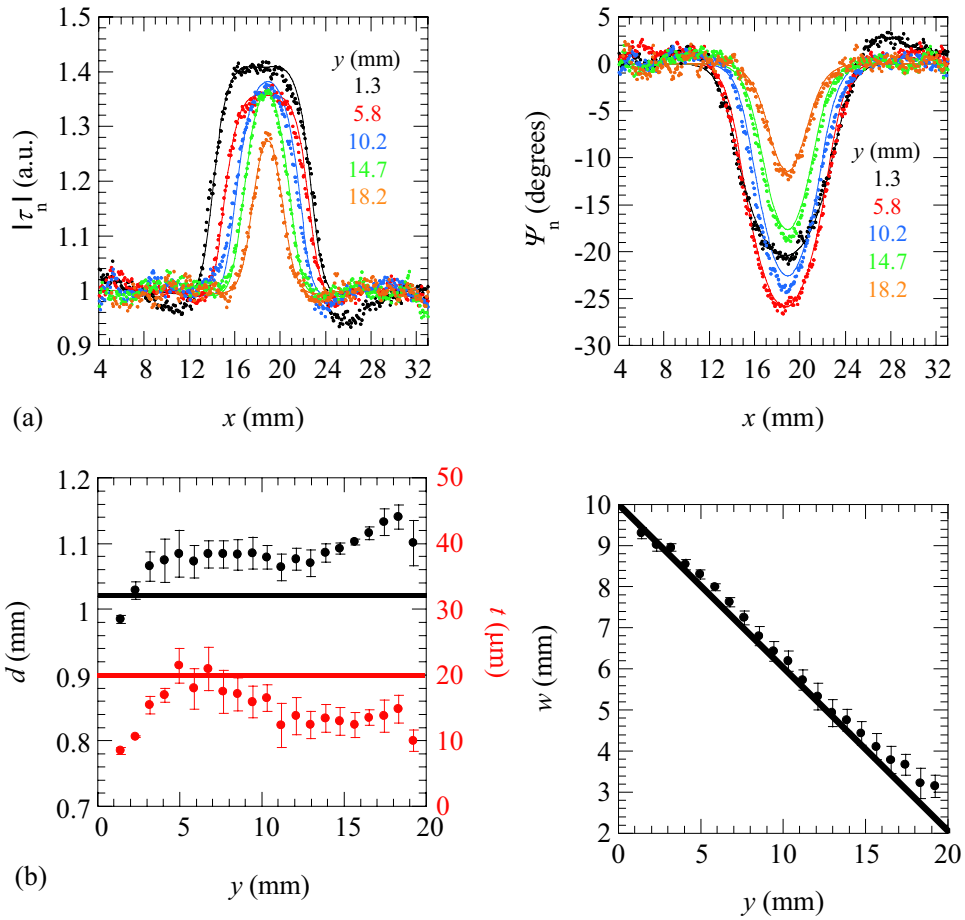

Fig. 5 Results for a delamination featuring constant depth ($d = 1.02$ mm) and thickness ($t = 20$ μm), but varying width from 2 to 10 mm. (**a**) Five experimental x-profiles of $|\tau_n|$ and Ψ_n, across the delamination (dots) at $f = 0.4$ Hz and fittings (solid lines). (**b**) Retrieved parameters of the delamination. Continuous lines represent the nominal values

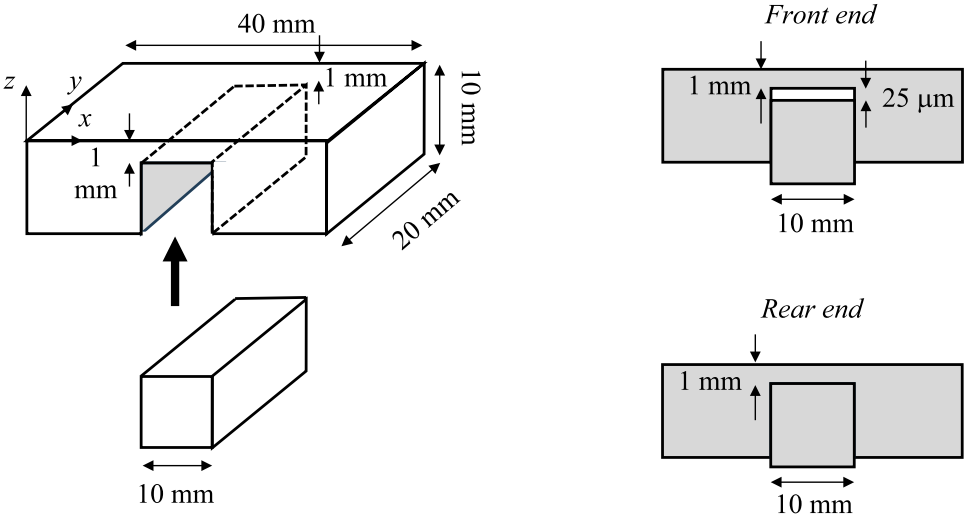

Fig. 6 Scheme of the AISI-304 U-shaped piece together with the tightly inserted part. The resulting delamination has fixed width, $w = 10$ mm, and depth, $d = 1$ mm, whereas the thickness continuously varies from $t = 25$μm to zero

Notice the very good agreement between nominal and measured values, with very low uncertainty. Anyway, it is worth discussing the amplitude and phase x-profiles for the position $y = 19.6$ mm (orange data in Fig. 8a). Note that the profiles show a clear asymmetry indicating that the thickness is not constant along the x-direction: it is slightly thicker on the right end of the delamination and thinner on the left end. However, the thickness variation is very small, perhaps about 1 μm between both ends. Given that the average fitted thickness is $t = 3$ μm, 1 μm difference

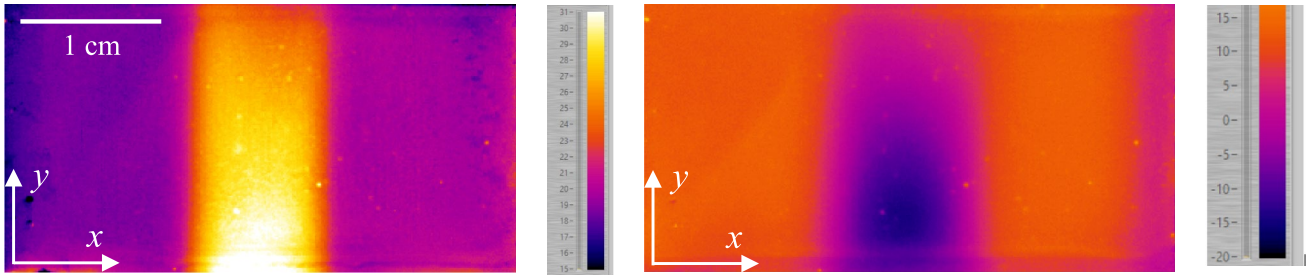

Fig. 7 Amplitude (left) and phase (right) thermograms at $f = 0.3$ Hz for the sample outlined in Fig. 6 with t continuously varying from 25 μm to zero

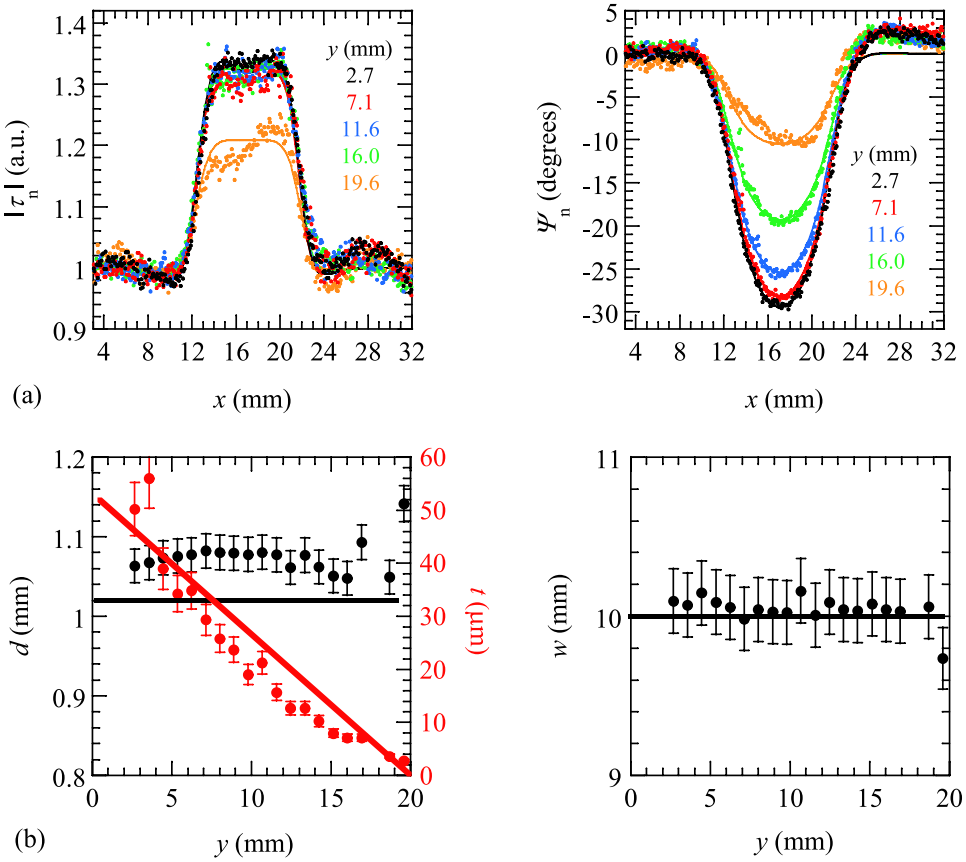

Fig. 8 Results for a delamination with fixed width ($w = 10$ mm) and depth ($d = 1.02$ mm), but variable thickness from 50 μm to zero. (**a**) Five experimental $|\tau_n|$ and Ψ_n profiles across the delamination (dots) obtained at $f = 0.4$ Hz, and fittings (solid lines). (**b**) Retrieved geometrical parameters of the delamination. Continuous lines are nominal values

in thickness represents about a 30% variation. This result confirms the theoretical prediction that thick delaminations (> 100 μm) are easy to detect but difficult to size because of the low sensitivity, while thin delaminations (< 10 μm) are difficult to detect, since they produce small temperature contrast, but easy to size because of their high sensitivity [22]. That is the reason why the uncertainty bars in t (red dots in Figs. 8b) for small values of this parameter are very short.

We have performed the same procedure for the same sample with t varying from 50 μm to zero. We have found very similar results, which are not shown here for the sake of succinctness.

3.4 Delamination with Wedge Depth

We manufactured delaminations with wedge depth in AISI-304 stainless-steel by eroding a U-shaped notch of constant width ($w = 10.0$ mm), but continuously varying thickness of the remaining roof, from 3 to 0.5 mm. An insert of the same material, which fits perfectly the inner surface of the U-shaped notch, is tightly introduced in the hole, as can be seen on the left part of Fig. 9. The thickness of the air layer was kept constant by means of two metallic films of the same thickness ($t = 20$ μm) placed at both ends of the hole. Note that both parts are larger than in the previous subsections.

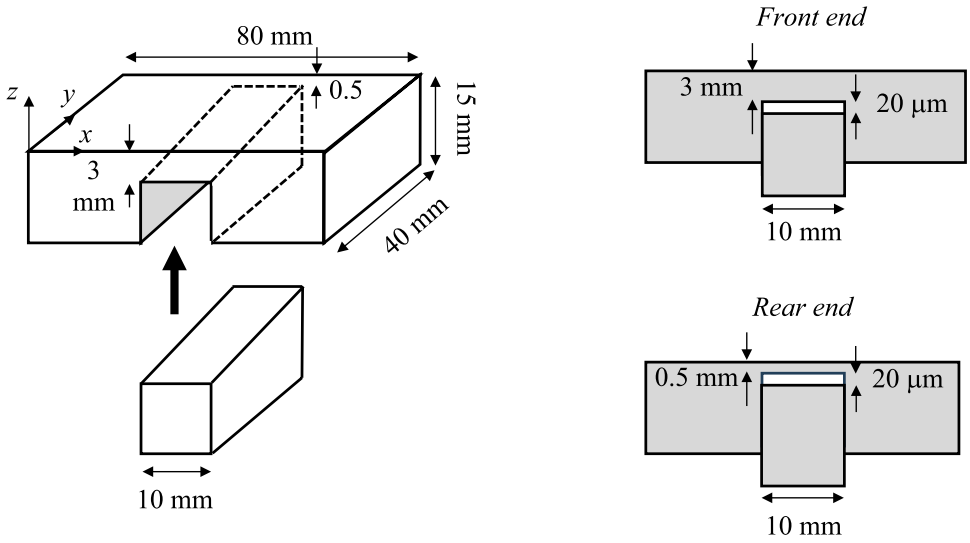

Fig. 9 Scheme of the AISI-304 stainless-steel part with a U-shaped notch together with the insert manufactured to obtain a calibrated delamination with fixed width $w = 10$ mm, fixed thickness $t = 20$ µm and wedge depth, varying from 3 to 0.5 mm

This was intended to have a smoothly varying depth in order to guarantee the validity of the 2D model.

To visualize the effect of the presence of a subsurface delamination with wedge depth, Fig. 10 displays amplitude and phase thermograms obtained at $f = 0.2$ Hz. Notice the variation of the contrast in both thermograms along the y-direction which, at first sight, could be ascribed to either t or d wedges. In Fig. 11a we show in dots five x temperature profiles at different y positions at $f = 0.2$ Hz. The continuous lines are the fit to the model. In Fig. 11b by dots we plot the retrieved average values of the geometrical characteristics of the delamination and by continuous straight lines the nominal values. We have used lower frequencies (0.05, 0.07, 0.1, 0.2 and 0.3 Hz) than in the two previous subsections in order to ensure that the thermal waves reach the deepest part of the delamination.

It is worth noting that the depth is obtained with high accuracy and low relative uncertainty. Regarding w and t, both are slightly overestimated. The reason for the overrated width values could be due to the influence of the lateral wall between the U-shaped piece and the insert. In fact, in this new sample there is a certain lateral clearance between both parts, which acts as an additional lateral thermal resistance not considered in the model. Concerning the retrieved thickness, it is remarkable the consistency of the results along the whole length of the delamination, i.e. there is not a reduction of precision when increasing the depth. Only the results for the deepest value (first point from the left in Fig. 11b) shows a small discrepancy with respect to the general trend probably due to border effects.

We have also taken data on the same sample with a thicker air layer ($t = 50$ µm) and we have obtained very similar results.

3.5 Delamination with Wedge Depth and Thickness

In this subsection we assess the ability of lock-in IRT to size delaminations when both depth and thickness vary slowly. In the first case d and t follow the same trend, i.e. decreasing d and decreasing t along the y-axis. Then, we study the opposite configuration: decreasing d but increasing t in the y-direction.

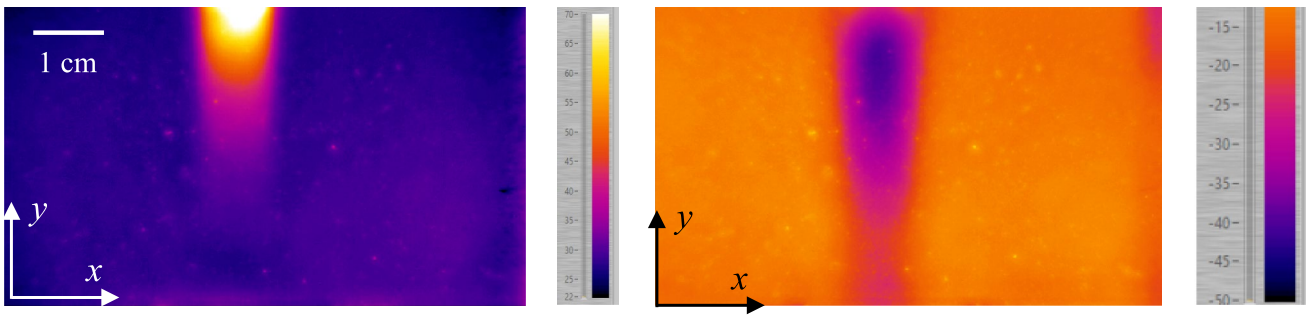

Fig. 10 Amplitude (left) and phase (right) thermograms at $f = 0.2$ Hz for the sample depicted in Fig. 9 with d continuously varying from 3 to 0.5 mm

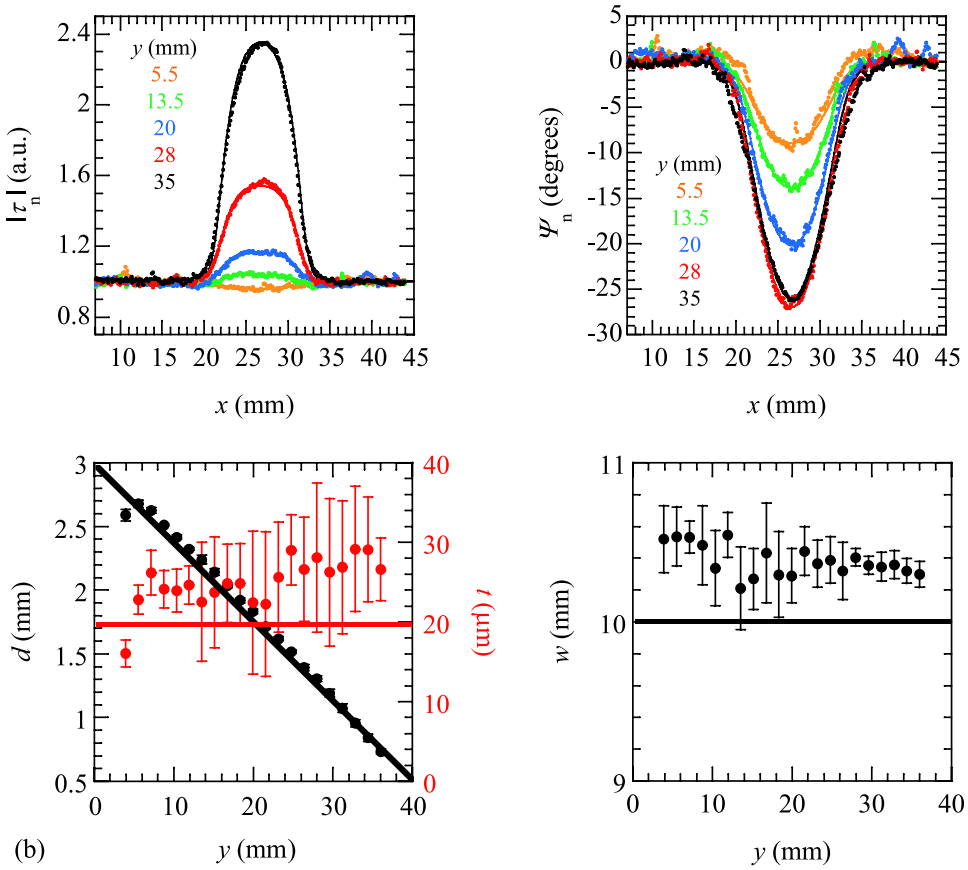

Fig. 11 Results for a delamination with fixed width ($w=10$ mm) and thickness ($t=20$ μm), but varying depth from 3 to 0.5 mm. (**a**) In dots, five experimental profiles of $|\tau_n|$ and Ψ_n across the delamination at $f=0.2$ Hz together with the fittings (continuous lines). (**b**) Retrieved geometrical parameters of the delamination. Continuous lines represent nominal values

3.5.1 Decreasing Depth and Thickness

We use the same couple of parts as in the previous subsection. However, the thickness varies from 100 μm to zero, as shown in Fig. 12, by putting the insert in contact with the notch at the rear end and introducing a metallic film 100 μm thick at the front end.

In Fig. 13 we show the amplitude and phase thermograms obtained at $f=0.1$ Hz. Note the expected contrast gradient along the y-direction in the amplitude thermogram. However, the phase thermogram is not so easy to interpret. In fact, the maximum contrast occurs in the middle of the thermogram. This is because the maximum contrast in amplitude and phase does not occur at the same frequency [10, 11].

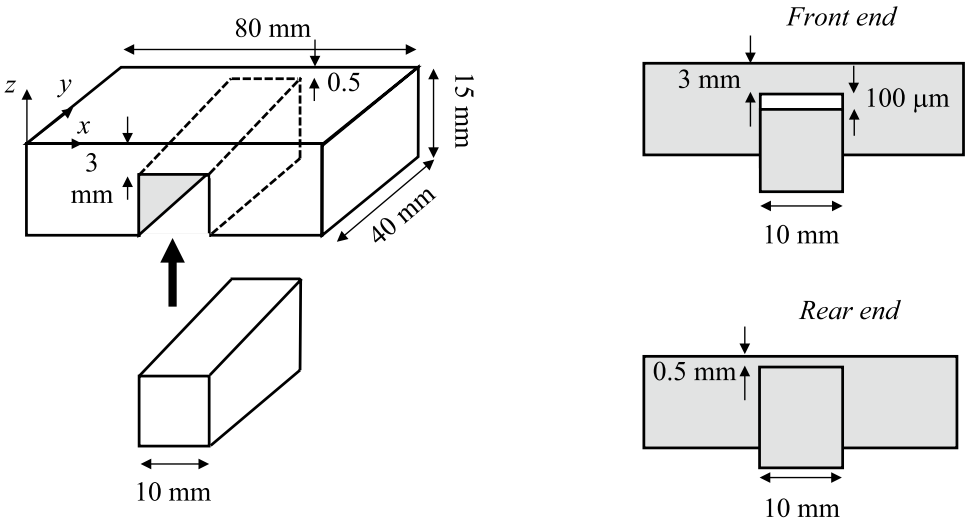

Fig. 12 Scheme of the AISI-304 stainless-steel U-shaped piece together with the insert to obtain a calibrated delamination with constant width $w=10$ mm, but wedge depth varying from 3 to 0.5 mm, and wedge thickness varying from 100 μm to zero, i.e., decreasing thickness for decreasing depth

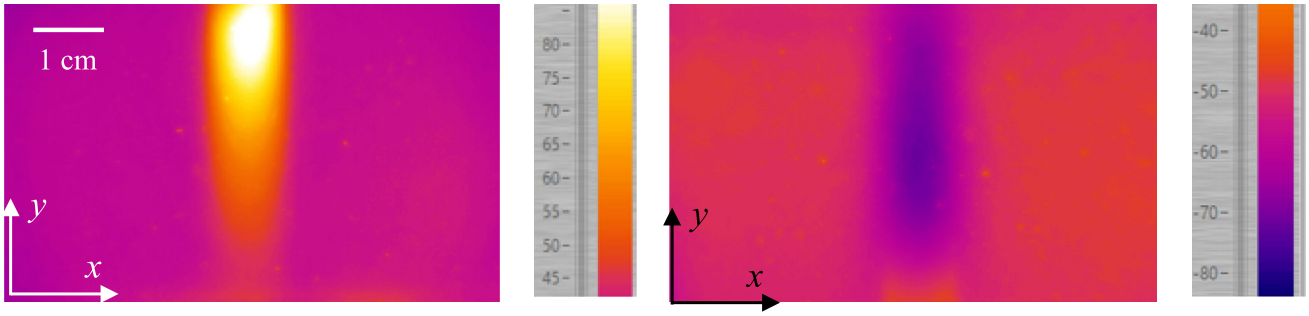

Fig. 13 Amplitude (left) and phase (right) thermograms at $f = 0.1$ Hz for the sample depicted in Fig. 12

This behavior is more evident when we look at the x temperature profiles across the delamination, as shown in Fig. 14a for the same frequency as in Fig. 13, $f = 0.1$ Hz. It can be observed that the amplitude contrast monotonously increases as both d and t decrease. However, phase contrast follows an oscillatory behavior, that is faithfully described by the model. Finally, in Fig. 14b we show by dots the retrieved mean values of the parameters characterizing the delamination and by continuous straight lines the nominal values. We use the same set of frequencies as in the previous subsection (0.05, 0.07, 0.1, 0.2 and 0.3 Hz).

Once again, the depth is obtained with high accuracy and low relative uncertainty in the whole delamination length. The thickness is well reproduced up to $t = 60$ μm and $d = 2.0$ mm. For deeper and thicker delaminations there is a progressive underestimation of this parameter. Although this disagreement between nominal and retrieved thicknesses might be ascribed to the deeper locations at which thick delaminations are located, as will be confirmed in the next subsection, it is due to the loss of sensitivity for thick delaminations: let us recall that they produce high contrast, and are thus easy to detect but the contrasts saturates, making them

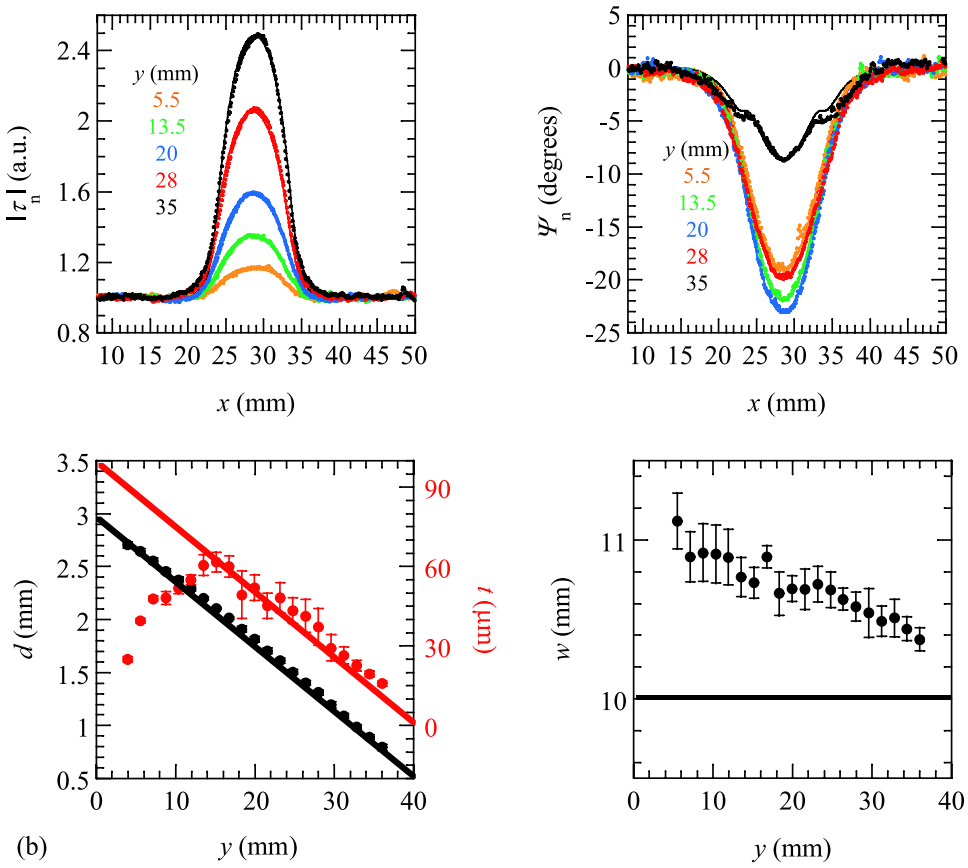

Fig. 14 Results for a delamination with fixed width ($w = 10$ mm) and wedge depth and thickness. (**a**) Experimental profiles of $|\tau_n|$ and Ψ_n (dots) across the delamination obtained at $f = 0.1$ Hz, and fittings (solid lines). (**b**) Retrieved delamination parameters. Continuous lines represent the nominal values

difficult to size [22]. Regarding the width, there is a systematic overestimation for the reason explained in the previous configuration: the lateral thermal mismatch between both metallic parts. Anyway, the overestimation is quite small, about 5–8%.

3.5.2 Decreasing Depth but Increasing Thickness

We use the same metallic parts as in the previous subsection, but the 100 µm thick film is put at the rear end. Accordingly, the thickness varies from zero to 100 µm along the *y*-axis, as shown in Fig. 15.

The amplitude and phase thermograms at $f = 0.1$ Hz are shown in Fig. 16. This result is very similar to that found in the previous case: the amplitude contrast is maximum at the shallowest depth, but the phase contrast is maximum in the middle. This behavior is clearly confirmed in Fig. 17a, which shows the temperature profiles across the delamination at the same frequency of $f = 0.1$ Hz. Note the very good agreement between data (dots) and model (continuous lines). In Fig. 17b we show by dots the retrieved mean values of the delamination parameters and by continuous straight lines the nominal values. We use the same set of frequencies as in subSect. 3.5.1 (0.05, 0.07, 0.1, 0.2 and 0.3 Hz). As can be observed, the depth is obtained with high accuracy and low relative uncertainty. The thickness is measured accurately for small values of this parameter (5—40 µm), even though they correspond to deep positions. However, for high values of thickness (50—100 µm) the accuracy is worse despite now they correspond to the shallowest positions. This result confirms the model's prediction that there is a high sensitivity for low thickness values (t in the range 5–50 µm) and that the sensitivity decreases as the thickness increases [22].

Finally, the width of the delamination is clearly overestimated by about 10%. However, the short error bars indicate that the uncertainty is very small. Looking at Fig. 11b, 14b and 17b, which are shown in chronological order of data taking, the overestimation of the delamination width is progressively enhanced. We think that it is due to an increase in clearance between the U-piece and the insert as it is introduced and

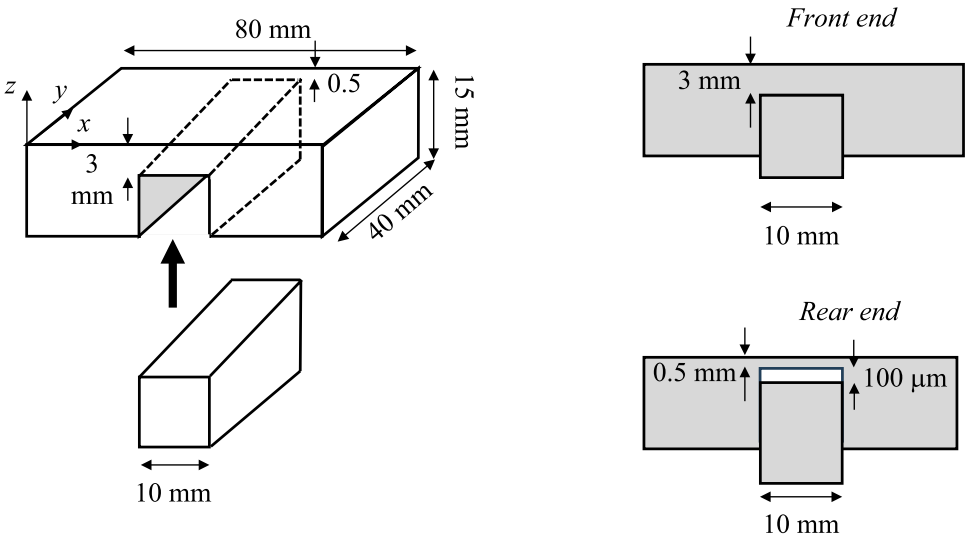

Fig. 15 Scheme of the AISI-304 stainless-steel U-shaped piece together with the insert to obtain a calibrated delamination with constant width $w = 10$ mm, but wedge depth varying from 3 to 0.5 mm, and wedge thickness varying from zero to 100µm, i.e., increasing thickness for decreasing depth

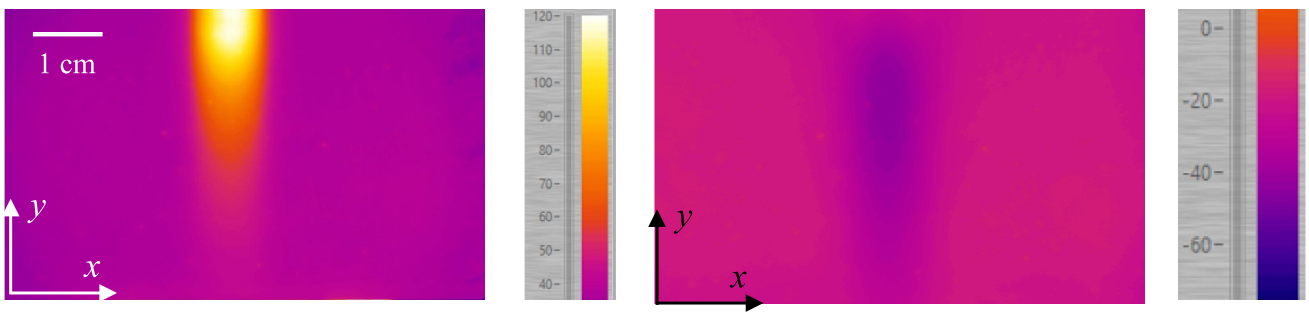

Fig. 16 Amplitude (left) and phase (right) thermograms at $f = 0.1$ Hz for the sample depicted in Fig. 15

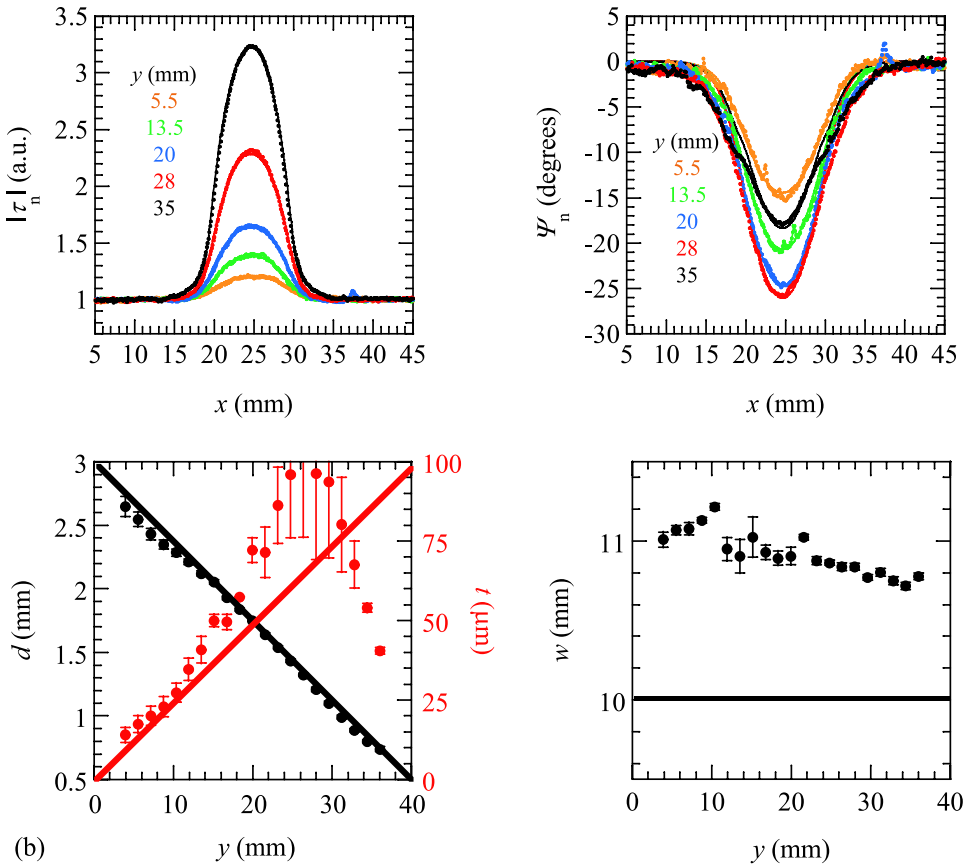

Fig. 17 Results for a delamination with fixed width ($w = 10$ mm) and wedge depth and thickness. (a) Experimental profiles of $|\tau_n|$ and Ψ_n across the delamination (dots) at $f = 0.1$ Hz and fittings (continuous lines). (b) Retrieved values of the parameters characterizing the delamination. Continuous lines represent the nominal values

extracted several times for successive experiments. Accordingly, in our opinion this overestimation is due to a manufacturing defect of the delamination rather than to a model deficiency. This opinion is supported by the fact that, according to Figs. 5b and 9b, which correspond to another smaller and more robust sample, the width is obtained with high accuracy and low uncertainty.

4 Conclusions

This paper on wedge delaminations completes previous works on semi-infinite delaminations, where we dealt with homogeneous as well as inhomogeneous thermal resistances of triangular cross-section. Elongated delaminations are expected to feature slowly varying geometrical properties and therefore the previously developed 2D model remains valid. The surface temperature is obtained analytically by means of the thermal quadrupoles' formalism and the cosine Fourier transform. A previous sensitivity analysis demonstrated that the three geometrical parameters are not correlated, i.e. the amplitude and phase temperature profiles at a given frequency correspond univocally to a single set of parameters (w,d,t).

The purpose of this work was to check experimentally the ability of lock-in thermography to size inhomogeneous semi-infinite delaminations with variable geometrical parameters (width, depth and thickness). We have performed lock-in IRT experiments on stainless-steel samples containing a variety of artificial and calibrated wedge delamination. The resulting amplitude and phase thermograms have been fitted to the predictions of the 2D model. The results show that this technique allows quantifying the three geometrical properties of the delamination with high accuracy when they vary independently, but also in cases where both depth and thickness vary simultaneously in the delamination.

We have also explored the limits of the technique in terms of capability of quantification depending on the depth and thickness of the delamination. It has been shown that in AISI 304- stainless steel, delaminations as deep as 3 mm can be sized accurately. In terms of thickness, counterintuitively it is easy to size thin delaminations (up to 50–60 μm in AISI-304), but the quantification of thicker flaws becomes a challenge because their high temperature contrast saturates. This maximum sizable thickness would be higher (lower) in materials of lower (higher) thermal conductivity. To the best of our knowledge, this is the first time that varying geometrical parameters of a semi-infinite delamination are quantified. These findings boost IRT as a reliable technique for the characterization of real delaminations.

Acknowledgements This work has been supported by Ministerio de Ciencia, Innovación y Universidades (Grant PID2023-146099OB-I00 funded by MCIU/AEI/https://doi.org/10.13039/501100011033/FEDER, UE) and by Departamento de Educación del Gobierno Vasco (IT1430-22).

Authors Contribution J.C. Ciria-Cosculluela: Investigation, Formal analysis, Software, Writing review & editing. J. Pérez-Arbulu: Investigation, Formal analysis, Writing review & editing. A. Mendioroz: Methodology, Investigation, Writing original draft. R. Celorrio: Conceptualization, Writing review & editing. A. Salazar: Methodology, Conceptualization, Supervision, Writing original draft.

Funding Open Access funding provided thanks to the CRUE-CSIC agreement with Springer Nature.

Data Availability The data that support the findings of this study are available from the corresponding author upon reasonable request.

Declarations

Competing interest The authors declare no competing interests.

References

1. Kachanov, L.M.: Delamination buckling of composite materials. Kluwer Academic Publishers, Dordrecht (1988)
2. Askaripour, K., Zak, A.: A survey of scrutinizing delaminated composites via various categories of sensing apparatus. J. Compos. Sci. **3**, 95 (2019)
3. Maldague, X.P.V.: Theory and practice of infrared technology for nondestructive testing. John Wiley & Sons, New York (2001)
4. Meola, C., Boccardi, S., Carlomagno, G.M.: Infrared thermography in the evaluation of aerospace composite materials. Woodhead Publishing in Materials, Elsevier (2017)
5. Vavilov, V., Burleigh, D.: Infrared thermography and thermal nondestructive testing. Springer (2020)
6. Tomita, K., Chew, M.Y.L.: A review of infrared thermography for delamination detection on infrastructures and buildings. Sensors **22**, 423 (2022)
7. Zhu, P., Wang, R., Sivagurunathan, K., Sfarra, S., Sarasini, F., Ibarra-Castanedo, C., Maldague, X., Zhang, H., Mandelis, A.: Frequency multiplexed photothermal correlation tomography for non-destructive evaluation of manufactured materials. Int. J. Extrem. Manuf. **7**, 035601 (2025)
8. Breitenstein, O., Langenkamp, M.: Lock-in thermography. Springer, Berlin (2003)
9. Salazar, A., Mendioroz, A.: Sizing the depth and thickness of ideal delaminations using modulated photothermal radiometry. J. Appl. Phys. **131**, 085106 (2022)
10. Salazar, A., Sagarduy-Marcos, D., Rodríguez-Aseguinolaza, J., Mendioroz, A., Celorrio, R.: Characterization of semi-infinite delaminations using lock-in thermography: theory and numerical experiments. NDT&E Int. **138**, 102883 (2023)
11. Sagarduy-Marcos, D., Pérez-Arbulu, J., Rodríguez-Aseguinolaza, J., Mendioroz, A., Batsale, J.C., Salazar, A.: Characterization of semi-infinite delaminations using lock-in thermography: experimental results. NDT E Int **138**, 102903 (2023)
12. Maillet, D., André, S., Batsale, J.C., Degiovanni, A., Moyne, C.: Thermal quadrupoles (Wiley, New York, 2000), chapter 6.2.
13. Bendada, A., Erchiqui, F., Lamontagne, M.: Pulsed thermography in the evaluation of an aircraft composite using 3D thermal quadrupoles and mathematical perturbations. Inverse Prob. **21**, 857 (2005)
14. Winfree, W.P., Zalameda, J.N., Howell, P.A., Cramer, K.E.: Simulation of thermographic responses of delaminations in composites with quadrupole method. Proc. SPIE **9861**, 98610N (2016)
15. Winfree, W.P., Zalameda, J.N., Howell, P.A.: Quadrupole simulations of three-dimensional structures. Proc. SPIE **11409**, 114090K (2020)
16. Pérez-Arbulu, J., Ciria, J.C., Mendioroz, A., Celorrio, R., Salazar, A.: Characterization of semi-infinite inhomogeneous delaminations using lock-in thermography. NDT&E Int. **155**, 103417 (2025)
17. Carslaw, H.S., Jaeger, J.C.: Conduction of heat in solids, 2nd edition, p. 20. Oxford University Press, Oxford (1959)
18. Arfken, G.B., Weber, H.J.: Mathematical methods for physicists, sixth edition, p. 939. Elsevier Academic Press, Amsterdam (2005)
19. Almond, D.P., Patel, P.M.: Photothermal science and techniques, p. 14. Chapman & Hall, London (1996)
20. Salazar, A.: On thermal diffusivity. Eur. J. Phys. **24**, 351 (2003)
21. Marín, E.: Thermal physics concepts: the role of the thermal effusivity. Phys. Teach. **44**, 432 (2006)
22. Sagarduy-Marcos, D., Batsale, J.-C., Rodríguez-Aseguinolaza, J.: Quantitative optimization analysis of lock-in infrared thermography for characterizing delaminations. Int. J. Heat Mass Transfer **231**, 125748 (2024)